

Unraveling the Electrochemical Mechanism in Tin Oxide/MXene Nanocomposites as Highly Reversible Negative Electrodes for Lithium-Ion Batteries

Antonio Gentile, Stefanie Arnold, Chiara Ferrara, Stefano Marchionna, Yushu Tang, Julia Maibach, Christian Kübel, Volker Presser,* and Riccardo Ruffo*

Lithium-ion batteries are constantly developing as the demands for power and energy storage increase. One promising approach to designing high-performance lithium-ion batteries is using conversion/alloying materials, such as SnO₂. This class of materials does, in fact, present excellent performance and ease of preparation; however, it suffers from mechanical instabilities during cycling that impair its use. One way to overcome these problems is to prepare composites with bi-dimensional materials that stabilize them. Thus, over the past 10 years, two-dimensional materials with excellent transport properties (graphene, MXenes) have been developed that can be used synergistically with conversion materials to exploit both advantages. In this work, a 50/50 (by mass) SnO₂/Ti₃C₂T_z nanocomposite is prepared and optimized as a negative electrode for lithium-ion batteries. The nanocomposite delivers over 500 mAh g⁻¹ for 700 cycles at 0.1 A g⁻¹ and demonstrates excellent rate capability, with 340 mAh g⁻¹ at 8 A g⁻¹. These results are due to the synergistic behavior of the two components of the nanocomposite, as demonstrated by ex situ chemical, structural, and morphological analyses. This knowledge allows, for the first time, to formulate a reaction mechanism with lithium-ions that provides partial reversibility of the conversion reaction with the formation of SnO.

1. Introduction

Rechargeable lithium-ion batteries (LIBs) are experiencing unprecedented success primarily due to the growing market penetration of electric vehicles (EVs). LIBs are the only technology capable of powering EVs today and will likely remain so for the next decades.^[1] However, to ensure better acceptance of the technology and to bridge the performance gap that remains with internal combustion engines, EV batteries must be even more efficient, safer, and less expensive than the current state-of-the-art. Cutting-edge LIB cells, called generation 3a, have gravimetric and volumetric energy densities of 250/300 mAh g⁻¹ and 700 Wh L⁻¹, respectively, with charging times of about 20 min and lifetimes of 1000 cycles (80% capacity retention).^[2] However, these performances seem difficult to overcome while maintaining the rocking chair operation principle that characterizes LIBs, based on the reversible

A. Gentile, S. Marchionna
Ricerca sul Sistema Energetico – RSE S.p.A.
Via R. Rubattino 54, Milano 20134 Italy

S. Arnold, V. Presser
INM – Leibniz Institute for New Materials
Campus D2.2, 66123 Saarbrücken, Germany
E-mail: volker.presser@leibniz-inm.de

S. Arnold, V. Presser
Department of Materials Science and Engineering
Saarland University
Campus D2.2, 66123 Saarbrücken, Germany

 The ORCID identification number(s) for the author(s) of this article can be found under <https://doi.org/10.1002/admi.202202484>.

© 2023 The Authors. Advanced Materials Interfaces published by Wiley-VCH GmbH. This is an open access article under the terms of the Creative Commons Attribution License, which permits use, distribution and reproduction in any medium, provided the original work is properly cited.

DOI: 10.1002/admi.202202484

C. Ferrara, R. Ruffo
Dipartimento di Scienza dei Materiali
Università di Milano Bicocca
Milano 20125, Italy
E-mail: riccardo.ruffo@unimib.it

C. Ferrara, R. Ruffo
National Reference Center for Electrochemical Energy Storage (GISEL)
Via G. Giusti 9, Firenze 50121, Italy

C. Ferrara, R. Ruffo
INSTM
Consorzio Interuniversitario per la Scienza e Tecnologia dei Materiali
Via G. Giusti 9, Firenze 50121, Italy

Y. Tang, J. Maibach, C. Kübel
Institute of Nanotechnology
Helmholtz Institute Ulm & Karlsruhe Nano Micro Facility
Karlsruhe Institute of Technology
Hermann-von-Helmholtz Platz 1, 76344 Eggenstein-Leopoldshafen,
Germany

V. Presser
Saarene – Saarland Center for Energy Materials and Sustainability
Campus D4.2, 66123 Saarbrücken, Germany

ion intercalation mechanisms at both electrodes. While it guarantees long lifetimes, it limits the specific energy, especially of the graphite-based negative electrode in almost all LIBs.

Moreover, already in generation 3a, a small quantity of conversion/alloying materials (5–7% of Si/SiO_x) have been introduced in the negative electrode to increase the specific capacity without compromising the mechanical integrity. To obtain superior performance for the next LIB generations, it is necessary to increase this quantity while simultaneously finding a way to contain the volume expansions inevitably associated with these compounds. Among different conversion/alloying materials, using SnO₂ or SnO_x has several advantages, such as the easy preparation routes and the large availability of raw materials. For example, the use of SnO₂ as an anode in LIBs dates back to 1997 when Jeff Dahn's group demonstrated the conversion/alloying reaction mechanism related to the insertion of lithium in glassy or crystalline SnO_x.^[3]



The mechanism can be described as an irreversible reduction of the oxide to metallic Sn with the formation of Li₂O (Equation (1)) followed by the reversible alloying/de-alloying reaction (Equation (2)).^[4] The amount of irreversible and reversible capacities depends on the oxygen content in the SnO_x and on the stoichiometry of the lithiated alloy, which in the case of tin, can be up to Li_{4.4}Sn. The approach was promising, and Fuji Film researchers were close to commercializing SnO_x-based electrodes able to provide 50% more capacity than carbon compounds.^[5] Later, the Schleich Group published seminal works on thin film crystalline SnO₂ electrodes, confirming the conversion/alloying mechanism, and revealing the morphological evolution of the system during cycling.^[6–8] It soon became clear that the limiting factor in the commercial application of these electrodes was the decrease of capacity during cycling due to the mechanical instability of the alloys and the volume expansion during the charge and discharge cycle, with loss of electric contact during cycling and electrode pulverization, a process defined as decrepitation.^[9] Two main routes have been explored to overcome this issue, namely nanostructuring of electrodes to allow expansion and contraction of the active material,^[10] and preparation of nanoscale composites, which in addition to buffering the volumetric changes, allow optimal electron distribution in the electrode bulk. In the former case, SnO₂ nanostructured fibers,^[11] porous structures,^[12,13] nanoparticles,^[14,15] hollow nanostructures,^[16,17] nanowires,^[18–20] and nanotubes^[21] have been prepared and characterized. Among the many composites investigated, however, the most interesting results were obtained with composites based on nanostructured carbons,^[21–28] graphene,^[29–35] metallic structures,^[36] and biopolymers.^[37] These works showed that nanostructured composites withstand a higher number of cycles, with performances often exceeding the theoretical limits calculated by combining the specific capacities of both SnO_x (according to Equations (1) and (2)) and the secondary phase (carbon, graphene, etc.). In combination with experimental evidence previously obtained by utilizing Mössbauer spectroscopy,^[38] this led to a revision of the electrochemical mechanism, attributing partial

reversibility to the conversion reaction (Equation (1)), which has been attributed to the oxidation reaction of freshly formed Sn by de-lithiation with Li₂O at the atomic scale. This is usually detected in differential capacity curves as belly-shaped peaks at potentials higher than 1 V.

Among the various two-dimensional conductive structures that can be used to improve the mechanical properties of conversion systems, MXenes have attracted interest in recent years. MXenes are a novel class of 2D layered transition metal carbides, nitrides, and/or carbonitrides with their combined properties such as good electronic conductivity, hydrophilicity, and flexibility.^[39–41] In particular, the Ti₃C₂T_z MXene phases have been recently used to produce composites with SnO₂ through different methods, such as self-assembly,^[42] atomic layer deposition,^[43] in situ quantum dots^[44,45] or nanoparticle formation.^[46,47] These works are characterized by performances that depend on the relative composition of the two phases, and which are concluded in a specific capacity range between 360^[47] and 700 mAh g⁻¹.^[43] The discrepancies are also related to the different cycling conditions and the different electrode charges. Despite these differences, in the charge and discharge profiles, there are common characteristics linked to the reaction potentials, which allow, through the differential capacity curves, to highlight the 3 main reactions, that is, the conversion of the oxide, the alloying of the tin and the intercalation in the MXene. Other common characteristics are the low Coulombic efficiencies in the first cycle, generally between 60%^[46] and 75%.^[45] At the same time, little information is available regarding the charge efficiency in the subsequent cycles, which does not exceed 98.5%.^[44,47] Despite these promising results, the progress in using this material combination for high-performance batteries has been stalled. This is because of the limited understanding of the intricate interaction between the oxide nanoparticles and the MXene and of the reaction mechanism when used as an anode in LIB.

In the present study, we show the possibility of preparing Ti₃C₂T_z/SnO₂ nanocomposite with excellent energy storage properties thanks to the intimate contact between the two components. With the idea of preparing nanocomposite with excellent reversibility properties, we limited the amount of tin oxide to 50% of the total mass, even if this choice may limit the specific capacity of the system. Moreover, we investigated the reversibility of the conversion reaction, highlighting, for the first time, the presence of amorphous SnO in the de-lithiated electrodes and proposing a coherent mechanism to explain the electrochemical data.

2. Results and Discussion

2.1. Materials Preparation

MXenes are suitable materials for preparing nanocomposites, and several strategies have been reported.^[48–51] In the present work, we prepared the desired nanocomposite following the procedure reported in **Figure 1a**. This synthesis was chosen both because it is capable of producing SnO₂ single-crystalline nanoparticles with dimensions on the order of a few nanometers,^[52] and because it can be carried out easily in the

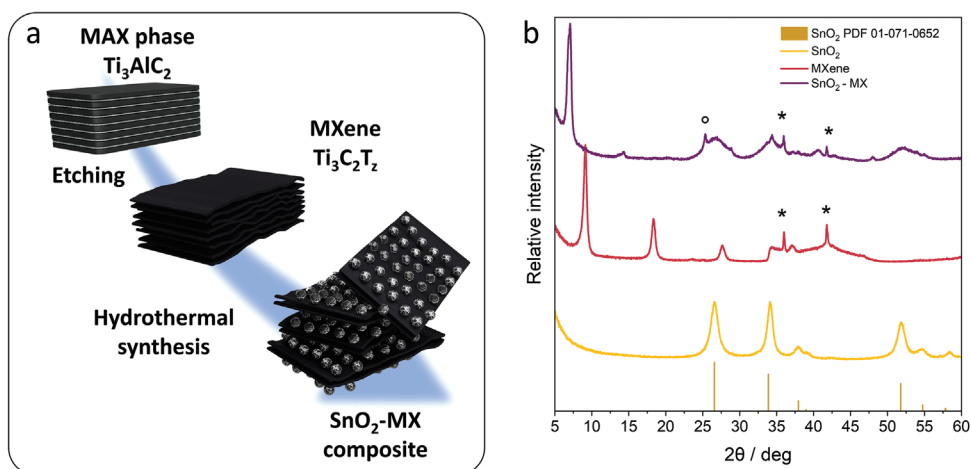


Figure 1. a) Scheme of the synthesis of the nanocomposite and b) X-ray diffractogram for the MXene (red), SnO₂ (yellow), and the nanocomposite (purple). Stars mark the TiC reflections; the circle marks the F-doped TiO₂ reflection.

presence of dispersed MXenes. The goal is to produce the nanoparticles directly on the surface of Ti₃C₂T_x layers by promoting their exfoliation during HCl evolution and thus maximizing the interaction between the nanoparticles and the MXene layers. A higher amount of oxide would have led to unacceptable values of Coulombic efficiency, while a decrease in it would have made the specific capacity of the nanocomposite of little application interest. Aiming to characterize the nanocomposite, the two components, Ti₃C₂T_x and SnO₂, have been carefully investigated to set the starting point for the subsequent analysis.

2.2. Materials Characterization

MXene was obtained by using HF-etching in high concentrations to obtain the well-known open-lamellae morphology.^[53,54] The obtained MXene structure is confirmed by the X-ray diffraction (Figure 1b). The collected data for the MXene are similar to those previously reported and discussed by our group and generally compliant with diffraction data of MXenes obtained with solution etching.^[51,55–58] The main features are the position of the (002) reflection at 9.1° 2θ related to the interlayer distance among the Ti₃C₂T_x layers and the blurring of the bands in the 30–50° 2θ region associated with the high level of disorder due to the presence of stacking faults and the distribution of the interlayer distances. Characteristic reflections of TiO_{2-x}F_x and TiC, as typical impurities for such type of synthesis, are also observed in the diffraction patterns.^[55,59–61] Scanning electron micrographs in **Figure 2a** show that the MXene presents the characteristic layered structure and microstructure, as already reported when high concentrations of HF and/or fast etching kinetic are exploited.^[53,55] This peculiar morphology was chosen because it was considered favorable for the intercalation of Sn ions during the immersion process in the tin chloride solutions and thus for the nucleation of the oxide on the surface of the lamellae. TEM investigations, reported in **Figure 2b**, and **Figures S1** and **S2** (Supporting Information), show the layered arrangement of the structure with extended disordered regions with variable interlayer distances, as also evidenced

by XRD. The EDX maps (**Figure S1**, Supporting Information) indicate the presence of Ti, C, F, and O compatible with the nominal MXene composition with mixed –F and –O terminations. Small traces of Al are also revealed but strongly localized and ascribable to AlF₃ and Al₂O₃ surface impurities, residues of the synthesis (**Table S1**, Supporting Information). O and F terminations are homogeneously distributed, indicating the absence of clustering. From the selected area electron diffraction (SAED; **Figure S2**, Supporting Information) it is also possible to detect the presence of surface TiO₂ and/or TiO_{2-x}F_{2x} nanoparticles, as already evidenced indirectly in our previous study.^[55] SAED also confirms the presence of a high level of 2D disorder. From the analysis of the radial distribution function (RDF) patterns,^[62,63] revealing the short-range structure, it is possible to detect the typical Ti–C (2.14 Å) and Ti–Ti (3.06 Å) distances expected for the parental MAX phase (comparison with the simulated data in **Figure S2**, Supporting Information) confirming that the etching procedure unaltered the Ti₃C₂ skeleton. Moreover, the obtained bond distances agree with those derived from the X-ray absorption spectroscopy (XAS) analysis performed on the same sample by our group.^[56] The additional peaks observed at 1.33 and 1.67 Å in the experimental RDF profile are ascribed to the O/F terminations interacting with trapped interlayer water molecules. This attribution is confirmed by the absence of such distances in the RDF profile of the MAX phase. The Ti–Ti bond distance is similar to the Ti–C distance, as already evidenced by XAS investigation, density functional theory (DFT), and pair distribution function (PDF) analysis.^[56,64,65] The surface chemistry has been characterized through XPS analysis (**Figure 3**). Both –F and –O terminations are observed, confirming the energy-dispersive X-ray (EDX) results. Titanium is observed in several oxidation states associated with different coordination with C, O, and F.^[55,61,66] The presence of surface TiO₂ is detected, again in agreement with previous observations.^[66,67]

To compare the results of the nanocomposite with the pristine material, it is also relevant to determine the structure, stoichiometry, and morphology of the tin oxide powders obtained via hydrolysis of the tin chloride. The diffraction

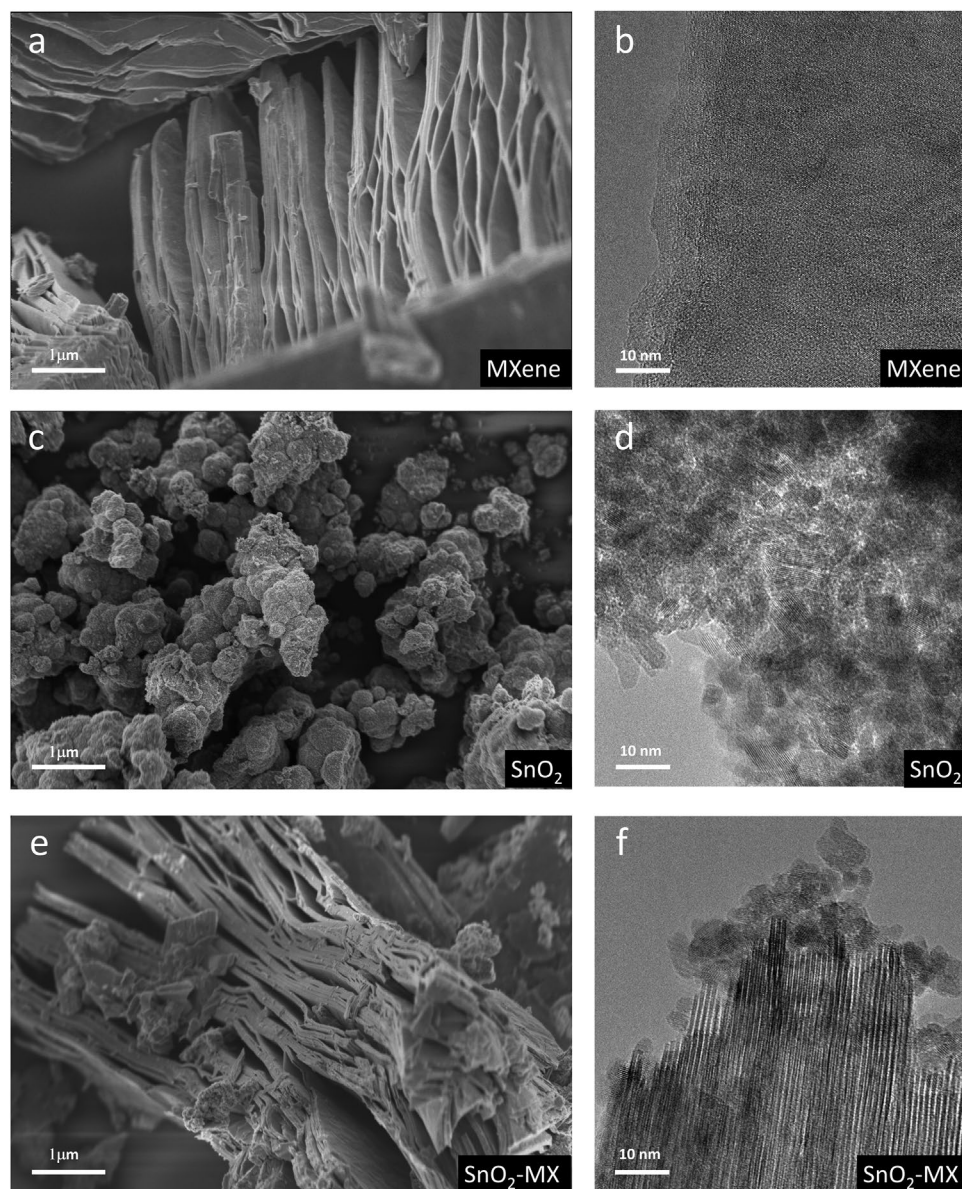


Figure 2. Scanning and transmission electron micrographs of a,b) MXene; c,d) SnO₂; e,f) SnO₂-MX nanocomposite.

pattern collected for the tin oxide powders (Figure 1b) is compatible with the cassiterite structure (PDF 01-071-0652), and the broadening of all reflections indicates that the powders are nanostructured; indeed, the size of the coherently scattering domains estimated from the two most intense XRD reflections is 8 ± 2 nm. This is also confirmed by the transmission electron microscopy (TEM) images (Figure 2d), revealing coherent crystalline domains of several nanometers, which tend to aggregate in secondary structures. Scanning electron micrographs (Figure 2c) reveal spherical agglomerates with a particle size of several hundred nanometers. The structural and morphological features can be further observed in TEM using diffraction (SAED) and energy dispersive X-ray spectroscopy (EDX), as represented in Figure S3 (Supporting Information), obtained on a single spherical agglomerate with a diameter of 350–400 nm. The diffraction pattern of such agglomerates reveals their

crystalline nature, with diffraction cones formed by many spots due to the random orientation of coherent crystalline domains. The surface chemistry has been investigated using XPS analysis, as reported in Figure 3. The analysis performed on the tin oxide powders suggests that the systems can be described as cassiterite SnO₂ and not as SnO, confirming XRD and TEM results.

The 50:50 nanocomposite, which represents the best compromise between higher specific capacity and reversibility of the electrochemical process, has been characterized by exploiting the same combination of techniques; results are reported in Figures 1–3. The X-ray diffractograms of the SnO₂-MX nanocomposite can be rationalized as the sum of the two components and indicates the successful synthesis of the nanocomposite (Figure 1b). Indeed, the main reflections of both the MXene and SnO₂ are still visible, indicating that the

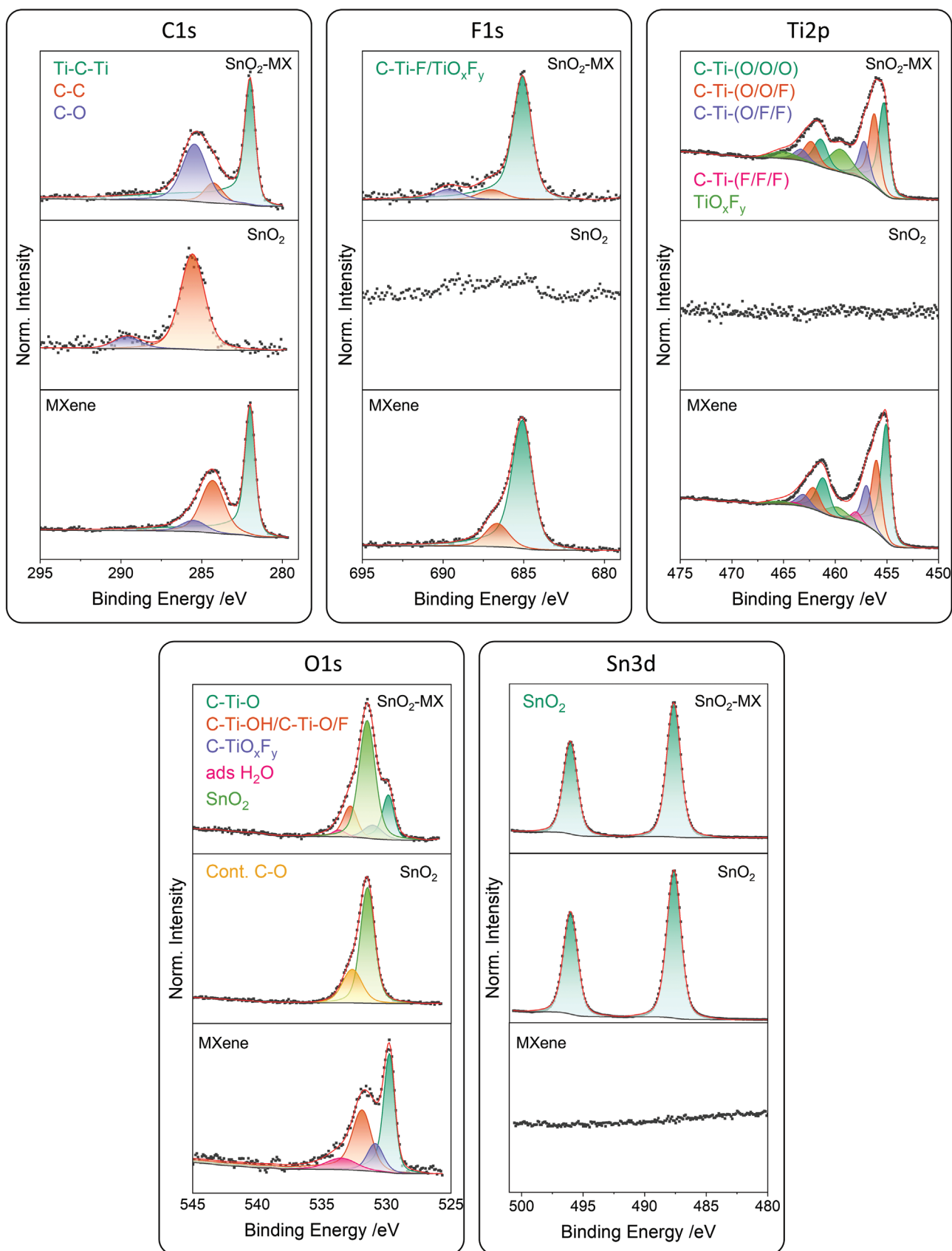


Figure 3. X-ray photoelectron spectra of the MXene, SnO₂, and the SnO₂-MX nanocomposite.

two structures are still present in the nanocomposite. At the same time, a significant shift at lower angles is observed for the 00l class of reflection of the MXene. In particular, the (002) reflection is downshifted to $6.9^\circ 2\theta$, indicating a widening of the interlayer distance moving from 9.6 to 12.6 Å. This can be related to the intercalation of Sn ions within the layers and/or the trapping of water molecules during the synthesis. The reflections of TiC and TiO₂ impurities are still visible; the amount of doped TiO₂ seems to be slightly increased for the pure MXene. This can be attributed to the open lamellar structure, which exposes a larger surface of the MXene layers, which are more susceptible to oxidation. Finally, it can be observed that the reflections attributed to the SnO₂ in the nanocomposite are broader than in the pure compound suggesting the formation of smaller particles of tin oxides when nucleating on the MXene surface. Similar evidence comes from electron microscopy. The nanocomposite clearly shows the presence of the two structures, as highlighted in Figure 2e,f. The open accordion-like structure of the MXene is present and unaltered by the preparation of the nanocomposite. SnO₂ particles with different degrees of aggregation can be observed on the MXene blocks (large clusters) and within the lamellae (small clusters). It is thus evident that the synthesis does not compromise the structure of the MXene and the SnO₂ powder. The SAED patterns confirm that the bond distances related to the Ti₃C₂ skeleton and the SnO₂ systems are the same as for the pristine materials. The EDX maps confirm the two components' homogeneous distribution and fine dispersion (Figure S4, Supporting Information). The XPS data obtained for the nanocomposite reveal that no strong surface modification has been introduced (Figure 3). The spectral region of oxygen in the nanocomposite appears as the superimposition of the contributions from the O-terminations of the MXene and the oxygen anions in SnO₂. At the same time, other elemental spectra are unaffected after the assembling procedure.

These results thus confirm the successful preparation of the 50:50 SnO₂-MX nanocomposite; the two components are present and unaltered. The fine dispersion of the two components is obtained at the nanometric level with the SnO₂ particles anchored on the MXene layers' surfaces.

2.3. Electrochemical Performance

For the sake of clarity, before discussing the electrochemical characteristics of the nanocomposite, the behaviors of pristine materials will be discussed (Figure S5, Supporting Information). Charge and discharge profiles and the resulting differential capacity curves were obtained in 3-electrode cells in all 3 cases, while long cycling of the nanocomposite was performed in two-electrode coin cells.

In pure SnO₂, the charge/discharge profiles (Figure S5a, Supporting Information) agree with the literature and are related to the conversion/alloying processes widely discussed in the introduction. The first cycle cathodic capacity is 1595 mAh g⁻¹, slightly higher than the theoretical value obtained considering the conversion reaction and the fully alloying to Li_{4.4}Sn (1493 mAh g⁻¹, 8.4 electrons per SnO₂ unit formula). The difference could be ascribed to the SEI

formation (starting below 1.3 V), also considering that the alloying reaction could be incomplete. The first cycle oxidation delivers 955 mAh g⁻¹, which corresponds to 5.4 electrons per unit formula, a value larger than the full delithiation of Li_{4.4}Sn to Sn (782 mAh g⁻¹). Moreover, a not negligible part of such capacity (250 mAh g⁻¹) is obtained at a potential >1.2 V, implying the partial reversibility of the conversion reaction and/or the reoxidation of the freshly formed SEI. The cycling properties of the SnO₂-based electrodes are very poor, with a capacity retention of 18% after 20 cycles (Figure S5c, Supporting Information). The specific capacity trend evidences the decrepitation of the electrode during oxidation, the cathodic capacity at a given cycle is practically equal to the anodic capacity at the previous cycle. The differential capacity curves help to better analyze electrochemical behavior (Figure S5b, Supporting Information). No reduction processes are detected up to 1.6 V during the first lithiation, while below this threshold, according to recent in situ characterizations,^[68] SnO₂ reacts to SnO and Li₂SnO₃. At around 1.0 V the main peak of the conversion reaction is observed, leading to the formation of metallic Sn and Li₂O. The further reduction peaks are attributed to the alloying between Sn and Li, with the following formation of intermediated phases such as LiSn, Li_{2.6}Sn, Li_{3.5}Sn, and Li_{4.4}Sn (cut off at 0.01 V). During the reoxidation, the peaks at 0.45 and 0.62 V are the footprint of the de-alloying reaction. In comparison, a further oxidative process (belly-shaped peak at 1.27 V) is detected, probably due to the partial conversion of Sn to SnO_x.

In pristine MXene, the charge/discharge profile (Figure S5d, Supporting Information) shows the already observed features first reported by Naguib et al. in 2012.^[69] Monotonic variation of the potential with the charge indicates a pseudocapacitive behavior during lithium-ion intercalation and de-intercalation. The specific cathodic and anodic capacities for the first cycle are 405 and 205 mAh g⁻¹, respectively, with a charge efficiency of 51%. The rate capability shows a good performance where the material can maintain a capacity from 120 mAh g⁻¹ at 500 mA g⁻¹ with excellent capacity retention of 99% after 70 cycles (Figure S5f, Supporting Information). The pseudocapacitive behavior is also seen in the differential capacity curves (Figure S5e, Supporting Information), which show a flat shape with little pronounced peaks after the first cycle which, instead, is characterized by the peaks of the SEI formation, the MXene stabilization, and the Li⁺ intercalation.

The electrochemical characteristics of the nanocomposites are reported in Figure 4. During these characterizations, the lower cut-off voltage was increased to 0.1 V because of the slight irreversibility of MXene reduction below this threshold, thus maximizing the electrode lifetime. The potential profiles (Figure 4a) reflect the behaviors of both active materials, showing the two main SnO₂ conversion/alloying processes (the latter is not complete due to the higher cut-off voltage) with a monotonic variation of the potential due to pseudocapacitive intercalation in MXene. The specific capacities for the first cycle are 1230 ± 70 mAh g⁻¹ and 695 ± 50 mAh g⁻¹, for the cathodic and the anodic scan, respectively, with a Coulombic efficiency of $56.5 \pm 3.5\%$ (data obtained with 4 different cells). The capacity profiles, the black curves in Figure 4b (first cycle) show in the cathodic process three main peaks related to the SEI

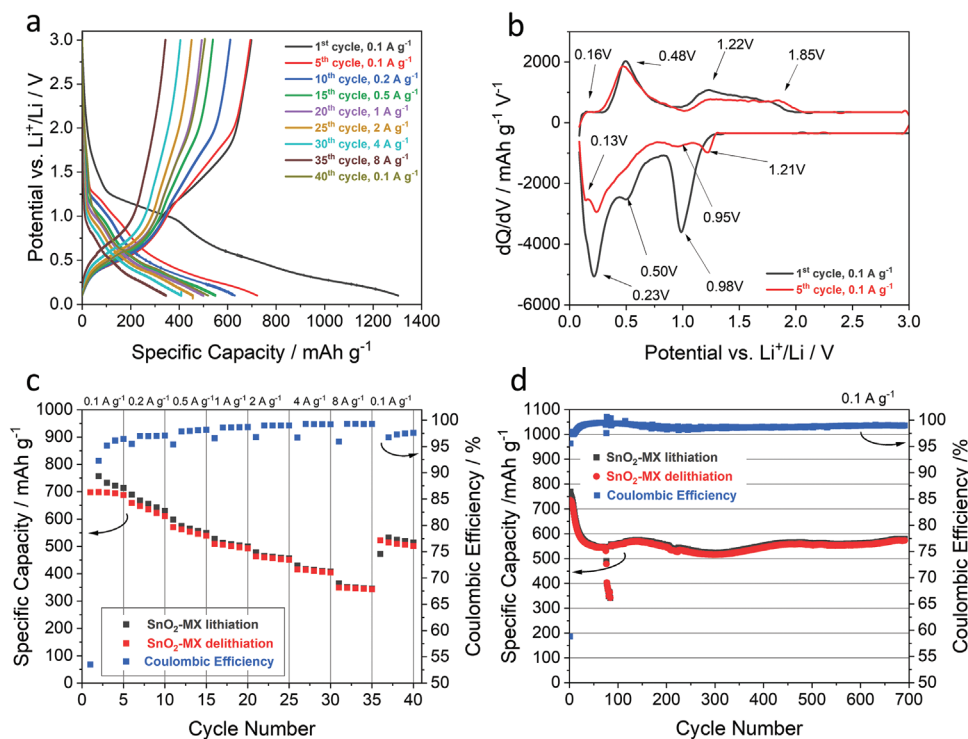


Figure 4. a) Charge–discharge profiles, b) differential capacity, c) rate capability test, and d) long-term stability test for SnO₂-MX nanocomposite as lithium-ion battery electrode.

formation, the conversion process, and the alloying of Sn with lithium. The first two processes happen at similar potentials and may be superimposed. During the successive oxidation, after the main process at 0.48 V (peak), which can be identified as the de-alloying reaction, a large amount of charge (around 300 mAh g⁻¹) is obtained at a potential higher than 1.0 V. This may be ascribed to the removing of lithium-ions from the MXene sheets; however, the presence of the peak at 1.22 V is not fully in agreement with the typical pseudocapacitive behavior of Ti₃C₂T_x, whose profile should be less pronounced.^[70,71] Since the conversion reaction (Equation (1)) should occur during the initial cycles, analyzing the differential capacity in the 5th cycle reveals essential information about the mechanism. Here (red curve in Figure 4b), during the reduction of the nanocomposite, a clear contribution to the capacity is present at a potential >0.75 V, with two peaks at 1.21 and 0.95 V. In this zone, the MXene is electroactive due to the Li⁺ intercalation in between the lamellae; however, the presence of the well-defined peak is an indication of a simultaneous phase transformation. The successive reoxidation shows a pseudocapacitive zone after the stable de-alloying reaction. In conclusion, the analysis of the differential capacity curves of the 5th cycle suggests the partial reversibility of the conversion reaction.

The three-electrode set-up was used to evaluate the kinetic performances of the nanocomposite/electrolyte interface (rate capability test) because the overvoltage at the Li⁺/Li counter electrode can affect specific capacity values at the highest currents increasing the real cut-off voltages of the working electrode. In the rate capability test (Figure 4c), the nanocomposite shows excellent properties, being able to sustain 450 mAh g⁻¹

at 2 A g⁻¹, 400 mAh g⁻¹ at 4 A g⁻¹, and 340 mAh g⁻¹ at 8 A g⁻¹. These values correspond to C-rate values of around 5, 10, and 20 C for commercial LIB negative electrodes with 400 mAh g⁻¹. This remarkable performance is probably the result of the synergistic interaction between the two materials. The long-term stability test (Figure 4d), performed in a coin cell in the low current regime (100 mA g⁻¹), which is normally a critical condition because secondary/degradation reactions have more time to occur, reveals that the material needs 50 cycles to stabilize the electrochemical performances. This effect has already been observed in the literature due to the initial decrease in Sn grain size formed by the conversion reaction with the loss of active material.^[72] Moreover, it has been proven that this results in a decrease of specific capacity until the Sn particles fall below a critical value that establishes greater reversibility in the conversion reaction, promoting the oxidation of more Sn to SnO by consuming Li₂O (see discussion in the next section). The tradeoff between Sn's fragmentation and the conversion reaction's reversibility is also the key to understanding the slow performance fluctuation observed from cycle 50 to cycle 700. In this cycle range, where the performance can be considered stable, an anodic capacity of 525 ± 25 mAh g⁻¹ with a charge efficiency of 98.8 ± 0.3% is observed. This represents a promising result considering the low current used during cycling and the use of commercial, non-optimized electrolyte. The stability test at 100 mA g⁻¹ lasted about 7700 h (over 320 days). Despite the long period and 700 cycles, the electrode showed no change in specific capacity from the stable values obtained after 50 cycles (100% capacity retention). In contrast, the first cycle capacity retention is 72%.

2.4. Ex Situ Analysis of Cycled Electrodes

A detailed characterization of selected cycled electrodes has been performed to identify the electrochemical behavior's origin and explain the electrochemical reaction's mechanism. Detailed chemical (XPS, EDX), structural (SAED), and morphological (STEM) characterizations have been performed on

cycled electrodes. XPS analysis has been carried out on electrodes collected from cells at the open-circuit voltage (OCV) and reduced to 1.0, 0.5, and 0.1 V. A further electrode was obtained after reoxidation to 3.0 V. Results are reported in **Figure 5**, and Figures S6 and S7 (Supporting Information). As demonstrated by our data, both nanocomposite components are electrochemically active. Indeed, both Ti and Sn regions

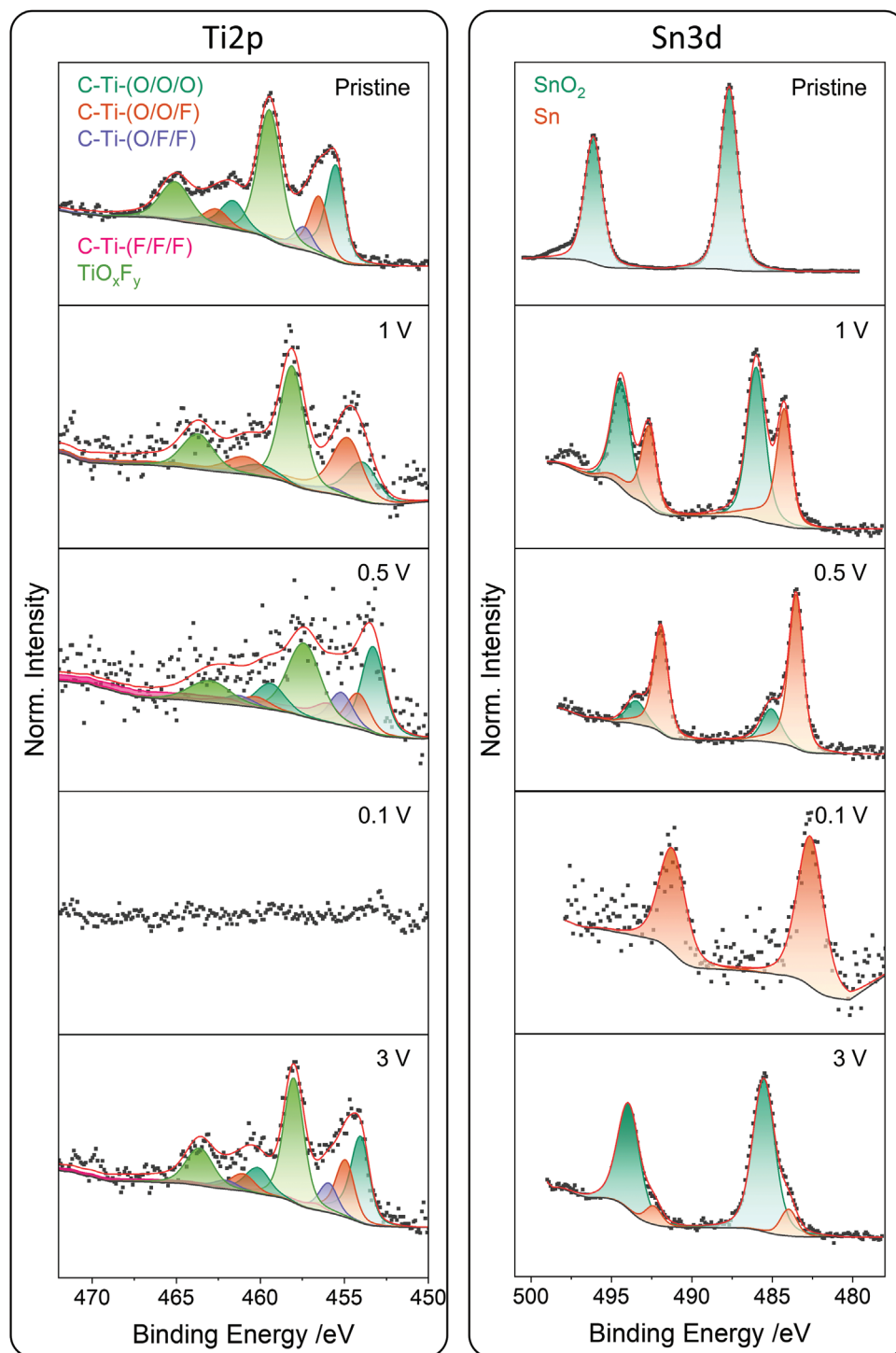


Figure 5. Ex situ Ti and Sn XPS spectra for electrodes cycled at different potentials.

(Figure 5) changed significantly upon cycling, but the two species behaved differently. The Ti region is characterized by different signals attributed to the different oxidation states and local coordination in the MXene phase, as already discussed in the first section. The evolution of this complex signal with lithiation is essentially a shift of all the components, attributed to the pseudocapacitive behavior of the MXene, already evidenced by a previous study.^[55] Due to SEI formation, the Ti 2p intensity drops significantly for low potentials but recovers in the de-lithiated state, indicating a dynamic SEI or surface layer that could contribute to the pseudocapacitive effect. The reoxidized electrode presents a Ti spectrum similar to the pristine compound, highlighting the reversible behavior of the MXene components. Contrary, the Sn region presents sharp changes with the appearance of new peaks for the electrode cycled to 1.0 V. From the OCV to this potential, a small lithiation of the SnO₂ is expected, with the tin oxide behaving like an insertion system for a very small fraction of Li.^[68] Below this potential, the reduction promotes the conversion reaction to Sn and Li₂O, attested by the appearance of the peak ascribed to metallic Sn (Figure 5).

Moreover, the contribution of Li₂O in the O 1s spectral region (Figure S6, Supporting Information) starts to appear at low energy (528.5 eV). These contributions (Sn and Li₂O) grow in intensity for the electrode reduced to 0.5 V and reach the highest intensities for the electrode reduced to 0.1 V. In this state, the component associated with Sn(IV) is not visible, suggesting the complete conversion of the tin oxide. Metallic Sn formed during the reduction can further lithiate at 0.1 V, forming various alloys. Based on the XPS results, it is impossible to distinguish among these different species as no suitable bulk-specific point of reference for the binding energy is present in the system. Although XPS is not the best tool to investigate alloying reactions, the Li 1s spectral region analysis provides information about the lithiation process, as further supported by STEM. A lithium peak (Figure S6, Supporting Information) appears at 1.0 V as the effect of the insertion reaction, and it shows the features of the characteristic Li⁺ in oxides or fluorides. However, as the alloying reaction proceeds (spectrum obtained at 0.1 V), a not negligible contribution is present at lower binding energy, as observed from the clear shoulder at 54.5 eV. This low energy contribution is usually associated with the higher electronic density of lithium bonded with less electronegative atoms, such as metallic Sn.

The analysis of the XPS for the electrode cycled to 3.0 V helps to understand the oxidation mechanism. The electrode's primary component in the Sn 3d spectrum cycled to 3.0 V shifts back to higher binding energies. However, compared to the electrode cycled to 1.0 V, a shift in binding energy toward lower binding energies remains, indicating that the conversion reaction is only partly reversible and the reoxidation does not produce SnO₂ but SnO_x. Additionally, a small shoulder at lower binding energies shows either incomplete reversibility of the conversion process or incomplete de-alloying. The signal related to Li₂O in the O 1s region is not observed at 3.0 V anymore, indicating that the tin reoxidation mechanism occurs at the expense of the lithium oxide formed during the conversion reaction. Finally, incomplete oxidation to SnO₂ and or de-alloying is also supported by the remaining Li intensity

at 3.0 V (Figure S6, Supporting Information), which, however, could also be incorporated in the SEI as LiF or other electrolyte decomposition products. This is further supported by the F1s and P2p regions (Figure S7, Supporting Information), where the decomposition of the LiPF₆ electrolyte salt can be observed. Traces of Na (not reported) are also observed due to the CMC binder used to prepare the electrodes. Given the absence of spectral variations in the Na 1s signal, we can exclude the Na as electrochemically active in the explored conditions.

To further characterize the conversion reaction and its reversibility, electrodes in the fully reduced state (0.1 V) and reoxidized to 3.0 V have been analyzed through (S)TEM, EDX, and SAED; the vacuum transfer holder was used to avoid contact with air; results on representative portions of such electrodes are reported in **Figure 6** and Figure S8 (Supporting Information). The fully reduced sample is unstable under the high-energy electron beam of HR-TEM, which induces the growth of metallic lithium. The STEM images collected for the 0.1 V cycled sample reveal that the electrode is mechanically stable after the alloying reaction. The elemental maps (EDX) of Sn and Ti show the intimate contact between the two materials, with the two elements homogeneously distributed in the corresponding phases. SAED results show that the external part of the MXene lamellae is covered with LiF nanometric particles formed as SEI. At the same time, the Sn-rich phase is compatible with the crystalline Li₁₃Sn₅ alloy, a direct demonstration of the alloying reaction. At the cut-off voltage of 0.1 V, the total composition should be Li₃Sn with the equilibrium between the Li₁₃Sn₅ and the Li₇Sn₂ alloys.^[73] This is in agreement with the phase observed by SAED, also considering that the two crystalline phases (Li₁₃Sn₅ and Li₇Sn₂) have very similar d-spacing. The analysis of the reoxidized electrode again highlights that the reaction does not involve a mechanical degradation of the nanocomposite, with the Ti and Sn EDX maps showing good homogeneity at the nanoscale level. The SAED analysis confirms the XPS results, indicating the conversion back to SnO. The analysis of the total diffraction data reveals that the conversion does not entirely restore the initial configuration as, together with SnO₂, it is possible to detect SnO in an amorphous state. On the contrary, the MXene component is stable and structurally unaltered by the reduction and oxidation reactions.

The electrochemical performance of our material is in line with SnO₂/MXene composites obtained with similar approaches (nanoparticles or other nanostructures on MXene sheets), as evident from **Table 1**. All the materials reported have low first-cycle charge efficiencies, require several cycles to reach stable performance, and show excellent lifetimes in half cells versus Li. However, as evident in the table, there is generally little attention to either the ratio of oxide to MXene or the Coulombic efficiency in subsequent cycles, which does not allow for a proper evaluation of the durability of full cells equipped with lithiated positive electrodes. In our case, these aspects have been carefully evaluated, and the 50/50 composition by mass was chosen as a compromise between increasing specific capacity and the reversibility of the electrochemical processes. The irreversible capacity value at the first cycle is an intrinsic characteristic of conversion materials related to oxide reduction. It often depends on the contact between the electrode surface and electrolyte, thus on the separator used and the type of cell.

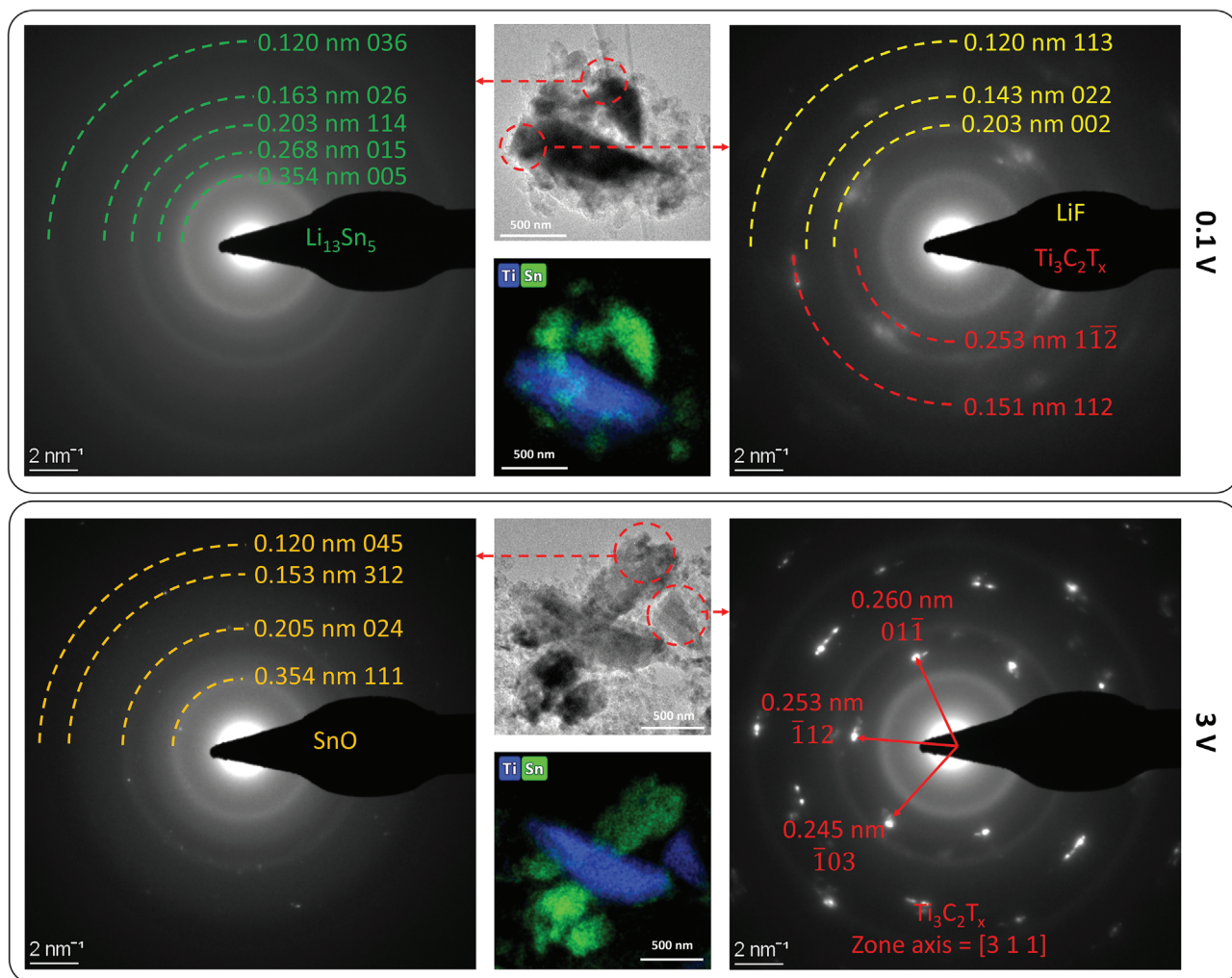


Figure 6. Ex situ STEM, EDS, SAED analysis for 0.1 and 3.0 V cycled electrodes.

In our case, we observed a marked increase from the custom-made cell to the coin cell. Methods to remedy this characteristic include chemical, and electrochemical pre-cycling, reductions by direct contact with lithium metal, or using sacrificial agents in the electrolyte.^[74]

3. Conclusions

Exploiting the possibility of preparing SnO₂ nanoparticles in the presence of Ti₃C₂T_x MXene, we successfully prepared a 50/50 mass% nanocomposite electrode able to provide an

Table 1. Comparison among the performances of different SnO₂/MXene composites. NR: not reported.

SnO ₂ ^{a)} morphology	SnO ₂ mass%	Anodic specific capacity 1st cycle [mAh g ⁻¹]	Coulombic efficiency 1st cycle	Stable anodic specific capacity [mAh g ⁻¹]	Coulombic efficiency	Number of cycles	Charge retention ^{b)}	Ref.
TLs	NR	1041	71%	900	NR	50	100%	[42]
NWs	70%	1700	NR	700	NR	500	100%	[43]
QDs	NR	960	73%	697	98.5%	700	100%	[44]
QDs	NR	637	61%	506	NR	160	98%	[45]
NPs	NR	961	60%	900	NR	1000	100%	[46]
NPs	NR	350	35%	350	98%	300	100%	[47]
NPs	50%	695	56%	525	98.8%	700	100%	This work

^{a)}TL = thin layer; NWs = nanowires, QDs = quantum dots, NPs = nanoparticles; ^{b)}Calculated after stabilization of the electrode.

anodic capacity of 525 mAh g⁻¹ for hundreds of cycles at low current over 10 months in lithium-ion battery half cell configuration. The electrode also shows promising kinetic properties, sustaining at 8 A g⁻¹ currents with a specific capacity of 340 mAh g⁻¹.

Due to the scarcity of chemical, morphological and structural data on such systems, we have used XPS and STEM to understand the electrode reactions better and elucidate the electrochemical mechanism. The results demonstrated that during the first cycle, the SnO₂ is converted to Sn first (Equation (1) in the Introduction) and Li₂O, while the formed Sn is then lithiated to the Li₁₃Sn₅ phase at a lower potential. Considering the amount of charge involved in the conversion reaction (711 mAh g⁻¹), in the alloying to Li₃Sn (533 mAh g⁻¹), and in MXene intercalation and stabilization (around 400 mAh g⁻¹), the total amount of charge at the first reduction of the 50–50% nanocomposite should be around 825 mAh g⁻¹. The excess of measured charge (417 mAh g⁻¹) could be due to the SEI formation or to the higher extension of the alloying reaction since, at the cut-off potential at 0.1 V, a higher amount of Li_{3.5}Sn may also be formed.

During the de-lithiation, the alloying reaction is mechanically stabilized thanks to the presence of the MXene sheets and the intimate interaction between the nanoparticles and the layered structure. Moreover, the conversion reaction becomes partially reversible, with the formation of amorphous SnO consuming part of the Li₂O following Equation (3):



Considering the amount of charge involved in Equation (3), the alloying to Li₁₃Sn₅, and the MXene contribution (100 mAh g⁻¹), the stable capacity of the nanocomposite should be around 545 mAh g⁻¹. This value, again, is less than the measured specific capacity of the first 25 cycles and may be influenced by the extension of the alloy lithiation. However, it agrees with the observed stable charge capacity during cycling (525 mAh g⁻¹).

Considering the overall performance, our nanocomposite material showed a high specific capacity, excellent capacity retention, and excellent rate capability. The charge storage properties are achieved due to the presence of tin oxide, while the reversibility and kinetics of the electrochemical reactions are due to the synergistic interaction between tin oxide and MXene, the latter being able to both act as a buffer for the conversion reaction and to enhance the charge transport properties in the electrode.

4. Experimental Section

MXene Preparation: MXene was prepared from the corresponding MAX phase of Ti₃AlC₂ by chemical etching. The MAX precursor was obtained by spark plasma synthesis using a procedure already described in the previous work, where a complete structural and morphological characterization of the precursor can also be found. The etching was done following the synthetic method used in previous work.^[55,75] The etching was performed using the following route: 500 mg of Ti₃AlC₂ (size <50 μm) was kept under stirring in a Teflon beaker containing an aqueous solution of hydrofluoric acid (HF) 30 mass% for 5 h at room temperature. The powder was recovered and washed by a series

of centrifugation steps until the pH of the washing liquid was ≈6. The resulting product was dried for 12 h under a vacuum at 80 °C.

Nanocomposite Preparation: The SnO₂-MX nanocomposite synthesis was carried out by modifying a synthesis protocol of SnO₂ nanopowders proposed in the literature.^[52] The synthetic scheme is shown in Figure 1. In a typical synthesis, 400 mg of SnCl₄·5H₂O (Sigma-Aldrich, 98% purity) was dissolved in 40 mL of deionized water. 170 mg of MXenes (Ti₃C₂T₂) were soaked overnight in this solution to promote the pre-intercalation of Sn ions into the 2D structure. The obtained solution was sonicated for 1 h, then 4 g of urea (Sigma-Aldrich, >99% purity), 8 mL of fuming HCl, and water were added under stirring (total volume was 160 mL). The solution was transferred into a Teflon-lined stainless-steel autoclave of 200 mL. The autoclave was sealed and maintained at 140 °C for 24 h. Finally, it was cooled down to room temperature in ambient conditions. The resulting white product was retrieved by centrifugation and washed several times with MilliQ water and absolute ethanol to reach a pH of 7. The powders were dried in a vacuum at 50 °C for 4 h.

To further investigate the system, tin oxide has been prepared as a pure compound following the same procedure reported without adding the MXene.

X-Ray Diffraction: X-ray diffraction measurements of the MXene nanocomposites were performed with a D2 PHASER diffractometer (Bruker AXS) with a copper X-ray source (Cu-K_α, λ = 1.5406 Å, 30 kV, 10 mA). The samples were measured in the range of 5 to 60 2θ deg and with 0.02 s per step.

Electron Microscopy: The morphology of the samples was characterized using Zeiss Gemini scanning electron microscope (SEM) equipped with a field emission source (FE-SEM). The electrons were accelerated using an electric potential of 1–5 kV for image acquisition. The samples were fixed on a steel sample holder using conductive carbon adhesive tapes. Scanning electron micrographs were analyzed using the ImageJ software.

The microstructure and elementary distribution of the samples were characterized by a probe-corrected Themis 300 transmission electron microscope (TEM; Thermo Fisher Scientific) equipped with a high-angle annular dark-field (HAADF) detector and a Super-X energy dispersive X-ray spectroscopy (EDX) detector. Selected area electron diffraction (SAED) was used to characterize the crystal structure of the samples. The measurements were carried out at an accelerating voltage of 300 kV. The pristine powder sample was dispersed on a TEM grid coated with holey carbon film. Samples of the cycled electrodes were scratched off using tweezers and dispersed on a TEM grid. The samples were transferred from a glove box into the TEM using a Gatan vacuum transfer holder (model number 648).

X-Ray Photoelectron Spectroscopy (XPS): XPS measurements were carried out using a K-Alpha spectrometer (Thermo Fisher Scientific), equipped with a micro-focused, monochromated Al K_α X-ray source (1486.7 eV) with 400-μm spot size. The data was recorded using a pass energy of 50 eV in the concentric hemispherical analyzer. To prevent sample charging during the analysis, the powder samples required K-α charge compensation system using a combination of both electrons and low-energy argon ions. Powder samples (MXene, SnO₂, SnO₂-MX nanocomposite) were measured as is and deposited directly on conductive copper tape. The electrodes were removed from the batteries at the desired state of charge and rinsed with DMC inside a glovebox to remove access electrolyte salts. To avoid reactions of the dried electrodes with air and moisture, the samples were transferred under Ar atmosphere to the spectrometer. Data acquisition and processing, using the Thermo Avantage software, as described in reference.^[66] The binding energy was referenced to C-Ti component at 282 eV for the powder samples containing MXene and to the hydrocarbon peak at 285 eV for all other samples, while the overall binding energy scale was controlled using well-known photoelectron peaks of metallic Ag, Au, and Cu. Data fitting followed the proposed model for MXenes described in reference^[66] using a smart background as implemented in the Thermo Avantage software.

Electrode Preparation: For the electrode preparation, a soft mixing method was used to preserve the morphology of the nanocomposites.

The 50/50-SnO₂-MX electrodes were manufactured by mixing the active material, conductive carbon, and carboxymethyl cellulose (CMC) in the ratio of 7:2:1. Firstly, the active material and carbon were mixed in a mortar. Afterward, the dry powder mix was dry-mixed at 1000 rpm for 5 min in a SpeedMixer DAC 150 SP from Hauschild. Milli Q water was added dropwise to the mixture until the slurry achieved suitable viscosity. This paste was again mixed at 1000 rpm for 5 min following 2500 rpm for 5 min. Finally, the CMC binder solution was added, and the viscous electrode paste kept mixing at 800 rpm for 10 min. The slurry was stirred for 12 h with a magnetic stirrer to obtain a homogeneous slurry. The slurry was spread with a doctor blade onto copper current collector foil (thickness of 9 μm, MTI) with an automatic coater (MTI Mini Cast Coater MSK-AFA-HC100), in a wet thickness of 200 μm. The electrode coatings were initially dried at room temperature overnight and in a vacuum at 110 °C for 12 h to remove the remaining solvent. The electrode was dry-pressed with a rolling machine (HR01 rolling machine, MTI), and finally, discs of 12 mm diameter were punched, resulting in a mass loading of the active material of ≈1.5 mg cm⁻².

Electrochemical Characterization: Custom-built polyether ether ketone (PEEK) cells with spring-loaded titanium pistons were used for electrochemical tests.^[76] After drying all cell parts at 120 °C for 14 h, the cells were assembled inside an Ar-filled glovebox (MBraun Labmaster 130; O₂ and H₂O < 0.1 ppm). The cells were arranged in a three-electrode configuration for electrochemical measurements, with the nanocomposites used as the working electrode and lithium metal as the counter and reference electrode. The electrolyte used was commercial LP30 (1 M LiPF₆ in ethylene carbonate and dimethyl carbonate (EC/DMC 50:50 by volume, Sigma-Aldrich)). All electrode potentials are reported versus the Li⁺/Li standard couple.

All electrochemical measurements were carried out in a climate chamber (Binder) with a constant temperature of +25 ± 1 °C. Rate performance measurements were conducted at different currents, in the potential window 0.1–3.0 V, to get more information about the half-cell rate capability and stability at higher currents. The applied specific currents were 0.1, 0.2, 0.5, 1.0, 2.0, 4.0, 8.0 A g⁻¹, and (again) 0.1 A g⁻¹.

The long-term stability tests were performed at 0.1 A g⁻¹. Two-electrode coin cells (2032-type) were used for these tests because they provide better sealing than PEEK cells, considering that the long-term tests lasted about one year due to the relatively low current, which provides more realistic results. All values obtained for cell capacity refer to the respective total active mass of the nanocomposite.

The cells were tested in a climatic chamber from BINDER with a constant temperature kept at 25 ± 1 °C, and the instruments used for the electrochemical analyses were a multichannel Bio-Logic VMP3 and an Arbin Battery Cycler.

Supporting Information

Supporting Information is available from the Wiley Online Library or from the author.

Acknowledgements

A.G. and S.A. contributed equally to this work. R.R. and C.F. acknowledge financial support from the Italian Ministry of University and Research (MIUR) through the Dipartimenti di Eccellenza – Materials for Energy. R.R. and A.G. acknowledge the financial support from the Research Fund for the Italian Electrical System under the Contract Agreement between RSE S.p.A. and the Ministry of Economic Development – General Directorate for the Electricity Market, Renewable Energy, and Energy Efficiency, Nuclear Energy in compliance with the Decree of April 16th, 2018. Y.T. acknowledges the financial support funded by the Deutsche Forschungsgemeinschaft (DFG, German Research Foundation) under Germany's Excellence Strategy – EXC 2154 – Project number 390874152 (POLiS Cluster of Excellence). Y.T., J.M., and C.K. acknowledge the

support of the Karlsruhe Nano Micro Facility (KNMFi, www.knmf.kit.edu, proposal-id 2020-025-030029), a Helmholtz Research Infrastructure at Karlsruhe Institute of Technology (KIT, www.kit.edu), and Center for Electrochemical Energy Storage Ulm-Karlsruhe (CELEST).

Open access funding enabled and organized by Projekt DEAL.

Conflict of Interest

The authors declare no conflict of interest.

Data Availability Statement

The data that support the findings of this study are available from the corresponding author upon reasonable request.

Keywords

alloying electrodes, conversion electrodes, lithium-ion batteries, MXene composite, SnO₂, Ti₃C₂T_z

Received: January 9, 2023

Revised: February 19, 2023

Published online:

- [1] D. Castelvetti, *Nature* **2021**, 596, 336.
- [2] E. Commission, *SET-Plan ACTION n°7 –Declaration of Intent “Become competitive in the global battery sector to drive e-mobility forward”*, https://setis.ec.europa.eu/implementing-actions/set-plan-documents_en, **2016**.
- [3] I. A. Courtney, J. R. Dahn, *J. Electrochem. Soc.* **1997**, 144, 2943.
- [4] I. A. Courtney, J. R. Dahn, *J. Electrochem. Soc.* **1997**, 144, 2045.
- [5] Y. Idota, T. Kubota, A. Matsufuji, Y. Maekawa, T. Miyasaka, *Science* **1997**, 276, 1395.
- [6] T. Brousse, R. Retoux, U. Herterich, D. M. Schleich, *J. Electrochem. Soc.* **1998**, 145, 1.
- [7] T. Brousse, *Solid State Ionics* **1998**, 113–115, 51.
- [8] R. Retoux, T. Brousse, D. M. Schleich, *J. Electrochem. Soc.* **1999**, 146, 2472.
- [9] R. A. Huggins, W. D. Nix, *Ionics (Kiel)* **2000**, 6, 57.
- [10] L. F. Nazar, G. Goward, F. Leroux, M. Duncan, H. Huang, T. Kerr, J. Gaubicher, *Int. J. Inorg. Mater.* **2001**, 3, 191.
- [11] N. Li, C. R. Martin, B. Scrosati, *J. Power Sources* **2001**, 97–98, 240.
- [12] A. Yu, R. Frech, *J. Power Sources* **2002**, 104, 97.
- [13] J. C. Lytle, H. Yan, N. S. Ergang, W. H. Smyrl, A. Stein, *J. Mater. Chem.* **2004**, 14, 1616.
- [14] H.-J. Ahn, H.-C. Choi, K.-W. Park, S.-B. Kim, Y.-E. Sung, *J. Phys. Chem. B* **2004**, 108, 9815.
- [15] S. Han, B. Jang, T. Kim, S. M. Oh, T. Hyeon, *Adv. Funct. Mater.* **2005**, 15, 1845.
- [16] X. W. Lou, Y. Wang, C. Yuan, J. Y. Lee, L. A. Archer, *Adv. Mater.* **2006**, 18, 2325.
- [17] Z. Wang, D. Luan, F. Y. C. Boey, X. W. (David) Lou, *J. Am. Chem. Soc.* **2011**, 133, 4738.
- [18] M.-S. Park, G.-X. Wang, Y.-M. Kang, D. Wexler, S.-X. Dou, H.-K. Liu, *Angew. Chem., Int. Ed.* **2007**, 46, 750.
- [19] P. Meduri, C. Pendyala, V. Kumar, G. U. Sumanasekera, M. K. Sunkara, *Nano Lett.* **2009**, 9, 612.
- [20] J. Y. Huang, L. Zhong, C. M. Wang, J. P. Sullivan, W. Xu, L. Q. Zhang, S. X. Mao, N. S. Hudak, X. H. Liu, A. Subramanian, H. Fan, L. Qi, A. Kushima, J. Li, *Science* **2010**, 330, 1515.

- [21] L. Li, X. Yin, S. Liu, Y. Wang, L. Chen, T. Wang, *Electrochem. Commun.* **2010**, *12*, 1383.
- [22] J. Fan, T. Wang, C. Yu, B. Tu, Z. Jiang, D. Zhao, *Adv. Mater.* **2004**, *16*, 1432.
- [23] F. Su, X. S. Zhao, Y. Wang, J. Zeng, Z. Zhou, J. Y. Lee, *J. Phys. Chem. B* **2005**, *109*, 20200.
- [24] Y. Wang, H. C. Zeng, J. Y. Lee, *Adv. Mater.* **2006**, *18*, 645.
- [25] X. W. Lou, D. Deng, J. Y. Lee, L. A. Archer, *Chem. Mater.* **2008**, *20*, 6562.
- [26] H.-X. Zhang, C. Feng, Y.-C. Zhai, K.-L. Jiang, Q.-Q. Li, S.-S. Fan, *Adv. Mater.* **2009**, *21*, 2299.
- [27] J. S. Chen, Y. L. Cheah, Y. T. Chen, N. Jayaprakash, S. Madhavi, Y. H. Yang, X. W. Lou, *J. Phys. Chem. C* **2009**, *113*, 20504.
- [28] J. Liang, C. Yuan, H. Li, K. Fan, Z. Wei, H. Sun, J. Ma, *Nano-Micro Lett.* **2018**, *10*, 21.
- [29] J. Yao, X. Shen, B. Wang, H. Liu, G. Wang, *Electrochem. Commun.* **2009**, *11*, 1849.
- [30] L.-S. Zhang, L.-Y. Jiang, H.-J. Yan, W. D. Wang, W. Wang, W.-G. Song, Y.-G. Guo, L.-J. Wan, *J. Mater. Chem.* **2010**, *20*, 5462.
- [31] X. Wang, X. Zhou, K. Yao, J. Zhang, Z. Liu, *Carbon N Y* **2011**, *49*, 133.
- [32] X. Zhou, L.-J. Wan, Y.-G. Guo, *Adv. Mater.* **2013**, *25*, 2152.
- [33] D. Wang, J. Yang, X. Li, D. Geng, R. Li, M. Cai, T.-K. Sham, X. Sun, *Energy Environ. Sci.* **2013**, *6*, 2900.
- [34] J. Sun, L. Xiao, S. Jiang, G. Li, Y. Huang, J. Geng, *Chem. Mater.* **2015**, *27*, 4594.
- [35] K. Zhao, L. Zhang, R. Xia, Y. Dong, W. Xu, C. Niu, L. He, M. Yan, L. Qu, L. Mai, *Small* **2016**, *12*, 588.
- [36] J. Deng, C. Yan, L. Yang, S. Baunack, S. Oswald, H. Wendrock, Y. Mei, O. G. Schmidt, *ACS Nano* **2013**, *7*, 6948.
- [37] B. Jiang, Y. He, B. Li, S. Zhao, S. Wang, Y.-B. He, Z. Lin, *Angew. Chem., Int. Ed.* **2017**, *56*, 1869.
- [38] I. A. Courtney, R. Dunlap, J. R. Dahn, *Electrochim. Acta* **1999**, *45*, 51.
- [39] B. Anasori, M. R. Lukatskaya, Y. Gogotsi, *Nat. Rev. Mater.* **2017**, *2*, 16098.
- [40] M. Naguib, M. Kurtoglu, V. Presser, J. Lu, J. Niu, M. Heon, L. Hultman, Y. Gogotsi, M. W. Barsoum, *Adv. Mater.* **2011**, *23*, 4248.
- [41] M. Naguib, M. W. Barsoum, Y. Gogotsi, *Adv. Mater.* **2021**, *33*, 2103393.
- [42] B. Ahmed, D. H. Anjum, Y. Gogotsi, H. N. Alshareef, *Nano Energy* **2017**, *34*, 249.
- [43] Y.-T. Liu, P. Zhang, N. Sun, B. Anasori, Q.-Z. Zhu, H. Liu, Y. Gogotsi, B. Xu, *Adv. Mater.* **2018**, *30*, 1707334.
- [44] J. Xiong, L. Pan, H. Wang, F. Du, Y. Chen, J. Yang, C. (John) Zhang, *Electrochim. Acta* **2018**, *268*, 503.
- [45] L. Wang, Y. He, D. Liu, L. Liu, H. Chen, Q. Hu, X. Liu, A. Zhou, *J. Electrochem. Soc.* **2020**, *167*, 116522.
- [46] C. Zhao, Z. Wei, J. Zhang, P. He, X. Huang, X. Duan, D. Jia, Y. Zhou, *J. Alloys Compd.* **2022**, *907*, 164428.
- [47] F. Wang, Z. Wang, J. Zhu, H. Yang, X. Chen, L. Wang, C. Yang, *J. Mater. Sci.* **2017**, *52*, 3556.
- [48] S. A. Jasim, J. M. Hadi, M. J. C. Opuencia, Y. S. Karim, A. B. Mahdi, M. M. Kadhim, D. O. Bokov, A. T. Jalil, Y. F. Mustafa, K. T. Falih, *J. Alloys Compd.* **2022**, *917*, 165404.
- [49] L. Biswal, R. Mohanty, S. Nayak, K. Parida, *J. Environ. Chem. Eng.* **2022**, *10*, 107211.
- [50] H. T. Das, T. E. Balaji, S. Dutta, N. Das, T. Maiyalagan, *Int. J. Energy Res.* **2022**, *46*, 8625.
- [51] C. Ferrara, A. Gentile, S. Marchionna, R. Ruffo, *Curr. Opin. Electrochem.* **2021**, *29*, 100764.
- [52] G. Xi, J. Ye, *Inorg. Chem.* **2010**, *49*, 2302.
- [53] M. Alhabeab, K. Maleski, B. Anasori, P. Lelyukh, L. Clark, S. Sin, Y. Gogotsi, *Chem. Mater.* **2017**, *29*, 7633.
- [54] M. Benchakar, L. Loupias, C. Garnerio, T. Bilyk, C. Morais, C. Canaff, N. Guignard, S. Morisset, H. Pazniak, S. Hurand, P. Chartier, J. Pacaud, V. Mauchamp, M. W. Barsoum, A. Habrioux, S. Célérier, *Appl. Surf. Sci.* **2020**, *530*, 147209.
- [55] A. Gentile, C. Ferrara, S. Tosoni, M. Balordi, S. Marchionna, F. Cernuschi, M. Kim, H. Lee, R. Ruffo, *Small Methods* **2020**, *4*, 2000314.
- [56] C. Ferrara, A. Gentile, S. Marchionna, I. Quinzeni, M. Fracchia, P. Ghigna, S. Pollastri, C. Ritter, G. M. Vanacore, R. Ruffo, *Nano Lett.* **2021**, *21*, 8290.
- [57] L. Verger, V. Natu, M. Carey, M. W. Barsoum, *Trends Chem.* **2019**, *1*, 656.
- [58] R. M. Ronchi, J. T. Arantes, S. F. Santos, *Ceram. Int.* **2019**, *45*, 18167.
- [59] R. B. Rakhii, B. Ahmed, M. N. Hedhili, D. H. Anjum, H. N. Alshareef, *Chem. Mater.* **2015**, *27*, 5314.
- [60] M. Naguib, V. N. Mochalin, M. W. Barsoum, Y. Gogotsi, *Adv. Mater.* **2014**, *26*, 992.
- [61] J. Halim, K. M. Cook, M. Naguib, P. Eklund, Y. Gogotsi, J. Rosen, M. W. Barsoum, *Appl. Surf. Sci.* **2016**, *362*, 406.
- [62] D. J. H. Cockayne, *Annu. Rev. Mater. Res.* **2007**, *37*, 159.
- [63] X. Mu, S. Neelamraju, W. Sagle, C. T. Koch, N. Totò, J. C. Schön, A. Bach, D. Fischer, M. Jansen, P. A. van Aken, *J. Appl. Crystallogr.* **2013**, *46*, 1105.
- [64] Q. Tang, Z. Zhou, P. Shen, *J. Am. Chem. Soc.* **2012**, *134*, 16909.
- [65] C. Shi, M. Beidaghi, M. Naguib, O. Mashtalir, Y. Gogotsi, S. J. L. Billinge, *Phys. Rev. Lett.* **2014**, *112*, 125501.
- [66] V. Natu, M. Benchakar, C. Canaff, A. Habrioux, S. Célérier, M. W. Barsoum, *Matter* **2021**, *4*, 1224.
- [67] J. Yang, M. Naguib, M. Ghidui, L. M. Pan, J. Gu, J. Nanda, J. Halim, Y. Gogotsi, M. W. Barsoum, *J. Am. Ceram. Soc.* **2016**, *99*, 660.
- [68] M. Mirolo, X. Wu, C. A. F. Vaz, P. Novák, M. El Kazzi, *ACS Appl. Mater. Interfaces* **2021**, *13*, 2547.
- [69] M. Naguib, J. Come, B. Dyatkin, V. Presser, P.-L. Taberna, P. Simon, M. W. Barsoum, Y. Gogotsi, *Electrochem. Commun.* **2012**, *16*, 61.
- [70] S. Fleischmann, J. B. Mitchell, R. Wang, C. Zhan, D. Jiang, V. Presser, V. Augustyn, *Chem. Rev.* **2020**, *120*, 6738.
- [71] S. Fleischmann, Y. Zhang, X. Wang, P. T. Cummings, J. Wu, P. Simon, Y. Gogotsi, V. Presser, V. Augustyn, *Nat. Energy* **2022**, *7*, 222.
- [72] P. Lian, X. Zhu, S. Liang, Z. Li, W. Yang, H. Wang, *Electrochim. Acta* **2011**, *56*, 4532.
- [73] M. Winter, J. O. Besenhard, *Electrochim. Acta* **1999**, *45*, 31.
- [74] V. Aravindan, Y. S. Lee, S. Madhavi, *Adv. Energy Mater.* **2017**, *7*, 1602607.
- [75] S. Arnold, A. Gentile, Y. Li, Q. Wang, S. Marchionna, R. Ruffo, V. Presser, *J. Mater. Chem. A* **2022**, *10*, 10569.
- [76] D. Weingarth, M. Zeiger, N. Jäckel, M. Aslan, G. Feng, V. Presser, *Adv. Energy Mater.* **2014**, *4*, 1400316.